21

An Attosecond Soft x-ray Nanoprobe: New Technology for Molecular Imaging

Sarah L Stebbings, Jeremy G Frey and William S Brocklesby
University of Southampton
United Kingdom of Great Britain and Northern Ireland

1. Introduction

The ability to image matter on the microscopic scale is of fundamental importance to many areas of research and development including pharmacology, materials science and nanotechnology. Owing to its generality, x-ray scattering is one of the most powerful tools available for structural studies. The major limitation however is the necessity of producing suitable crystalline structures – this technique relies upon many x-ray photons being scattered from a large number of molecules with identical orientations. As it is neither possible nor desirable to crystallise every molecule of interest, this has provided a huge drawback for most biotechnologies. Although improvements in both sources and detectors have had a strong impact in this area, driving down the required sample size, the need for macroscopic crystalline samples remains a fundamental bottleneck. Fortunately recent technological developments in the generation and sub-micron focusing of soft x-rays (SXRs) have provided a route for bypassing the need for a regular, crystalline structure.

For the purposes of this chapter, SXRs are defined as electromagnetic radiation with wavelengths from 1 – 50 nm, which correspond to photon energies of 1.2 keV – 25 eV respectively. As their wavelengths are on a comparable scale to objects such as proteins, cells and quantum dots, SXRs are ideally suited for imaging these targets with a high spatial resolution. Furthermore water is transparent and carbon opaque to SXRs whose wavelengths lie between 2 – 4 nm, the so-called water window. This offers clear potential for the imaging of biological molecules within their native, aqueous environment, something that would be impossible using traditional x-ray crystallography experiments.

Unsurprisingly there has been great interest in the production and application of SXRs across a wide range of scientific endeavours including, but not limited to, resolving electron motion (Drescher et al. 2002), production of isolated attosecond pulses (Goulielmakis et al., 2008) and x-ray diffraction microscopy (Sandberg et al., 2008). To date there are three major approaches employed to generate SXRs.

The free electron laser (FEL) such as the one located at DESY, Hamburg in Germany, exploits the interactions of electrons within an alternating magnetic field to produce SXR radiation. Electrons are accelerated up to relativistic speeds before being passed into undulator. The undulator consists of a series of magnets that produce an alternating field that causes the electrons to oscillate and emit SXR radiation. These electrons are then able to interact with the radiation to form micro bunches leading to a significant increase in the SXR intensity. Using this source, researchers have produced some impressive images via

Source: Advances in Solid-State Lasers: Development and Applications, Book edited by: Mikhail Grishin,
ISBN 978-953-7619-80-0, pp. 630, February 2010, INTECH, Croatia, downloaded from SCIYO.COM

holographic (Rosenhahn et al., 2009) and diffraction techniques (Bogan et al., 2008). Due to the properties of the SXR source, the objects that were being imaged were destroyed after only one laser "shot". This is unfortunate as it places a major limitation on the potential quality and reproducibility of the data.

A second approach is to employ a synchrotron source such as the Diamond light source at the Rutherford Appleton Laboratory in Oxfordshire, UK. Here electrons are accelerated up to relativistic speeds in a linear accelerator, booster synchrotron and storage ring. There are a series of bending magnets within the storage ring that control the electron trajectories and cause them to emit synchrotron radiation. This radiation typically ranges from the infrared (wavelength, λ = 700 nm) to gamma rays ($\lambda = 10^{-3}$ nm), easily encompassing the SXR range of the electromagnetic spectrum. Further arrays of magnets within the storage ring cause the electrons to wiggle in a similar manner to the undulator in a FEL, resulting in a more tuneable and intense light beam. The generality of this source has been demonstrated in recent work investigating the structure of metallic nanowires (Humphrey et al., 2008) and the characterisation of 3D molecular orbitals (Beale et al., 2009). In common with FELs, synchrotrons are multi-user, large-scale facilities whose cost and beam time can be restrictive to many researchers. Fortunately there is a third approach to producing SXRs that is a fraction of the cost and can fit in a standard size laboratory.

This chapter describes the development and implementation of such a source of sub-femtosecond (1 fs = 10^{-15} seconds) SXR duration pulses that can be focused down to the nanometre (1 nm = 10^{-9} metres) scale. Consequently this source has the potential to reach down in scale in both time and space that are of enormous benefit to a wide range of fields such as engineering, physical and biological sciences, significantly extending upon the generality of traditional x-ray scattering experiments. In contrast to the synchrotron and FEL sources, this source exploits the highly nonlinear interaction between an intense, femtosecond laser field with a gas medium such as argon in order to produce SXR radiation via a process known as laser-driven high harmonic generation.

2. Semi-classical and quantum mechanical approaches to high harmonic generation

Laser-driven high harmonic generation is an effective and relatively cheap way in which to produce SXRs using an intense laser field and a gas medium such as argon. It is a highly nonlinear process which can most easily be understood in terms of the so-called three step model (Corkum, 1993; Schafer et al., 1993; Lewenstein et al., 1994). In this model the combination of the intense laser field with the atomic potential increases the tunnelling probability of the valence electron through the modified potential barrier as shown in figure 1(a). This electron is then accelerated by the laser field while in the continuum, figure 1(b). In the case of a linearly polarised laser field, the electron will subsequently be driven back to its parent ion when the field reverses direction as shown in figure 1(c). This process occurs every half cycle of the laser pulse – multi cycle driving laser pulses will result in a series of SXR photon bursts which will coherently interfere. Fourier transforming this interference yields the characteristic high harmonic spectrum (Stebbings et al., 2008). The spectrum is a comb of frequencies up to a maximum energy known as the cut-off, E_{max}, is given by equation (1).

$$E_{\max} = I_p + 3.17U_p \approx \lambda^2 I \tag{1}$$

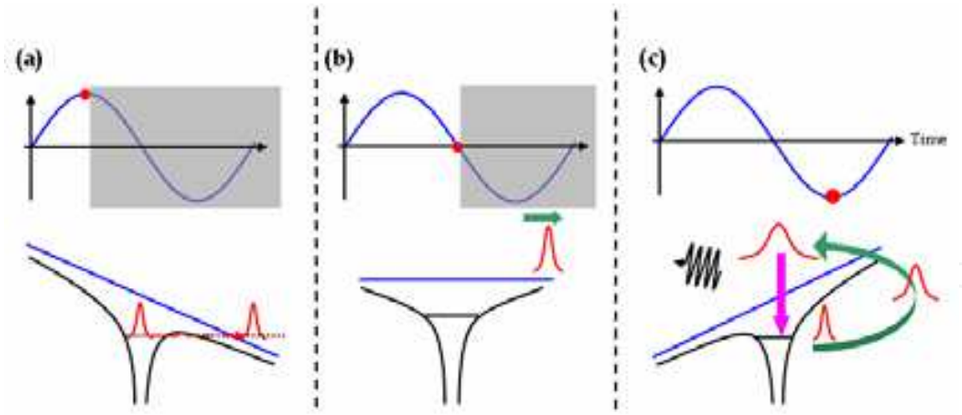

Fig. 1. Semi classical 3 step model of laser-driven high harmonic generation: (a) tunnel ionisation followed by (b) acceleration within the continuum and (c) recombination and emission of an SXR photon. The valence electron is shown in red and the time-dependent evolution of the laser field along with its effect on the atomic potential is shown in the top and bottom panels respectively.

Where I_p is the ionisation potential of the valence electron, U_p is the pondermotive potential, λ and I are the laser wavelength and intensity respectively.

Although the semi-classical model allows much of the underlying physics of high harmonic generation to be understood, it is necessary to solve the time-dependent Schrödinger equation (Jordan & Scrinzi, 2008) in order to fully describe the behaviour of a single atom within an intense, ultrafast laser field. Starting with a simple one dimensional time-dependent Schrödinger equation, a "soft" Coulomb potential is used as described by equation 2.

$$V \propto \frac{1}{\sqrt{x^2 + a_0^2}} \tag{2}$$

The next step is to solve the time-independent Schrödinger equation

$$H\psi = E\psi \tag{3}$$

in order to create a ground state wavefunction. This wavefunction is then allowed to propagate in time in the presence of the applied laser field. The final step is to carry out a numerical integration using the Crank-Nicholson scheme in order to solve equation 4

$$i\frac{h}{2\pi}\frac{d\psi}{dt} = \frac{h^2}{2m}\frac{d^2\psi}{dt^2} + \left(V_{static} + V_{laser}\right)\psi \tag{4}$$

and yield the electron acceleration as a function of time which is then Fourier transformed to give the theoretical high harmonic SXR spectrum.

This model was applied to an atom within a laser field of intensity, I = 3 x 10^{14} W/cm^2 for pulse durations of 30 fs and 7 fs, the results of which can be seen in figures 2 (a) and (b) along with the corresponding high harmonic spectra in figures 2 (c) and (d) respectively.

As can be seen in figures 2 (a) and (b), part of the valence electron wavefunction is ionised into the continuum at specific times during the optical cycle of the laser pulse, while a

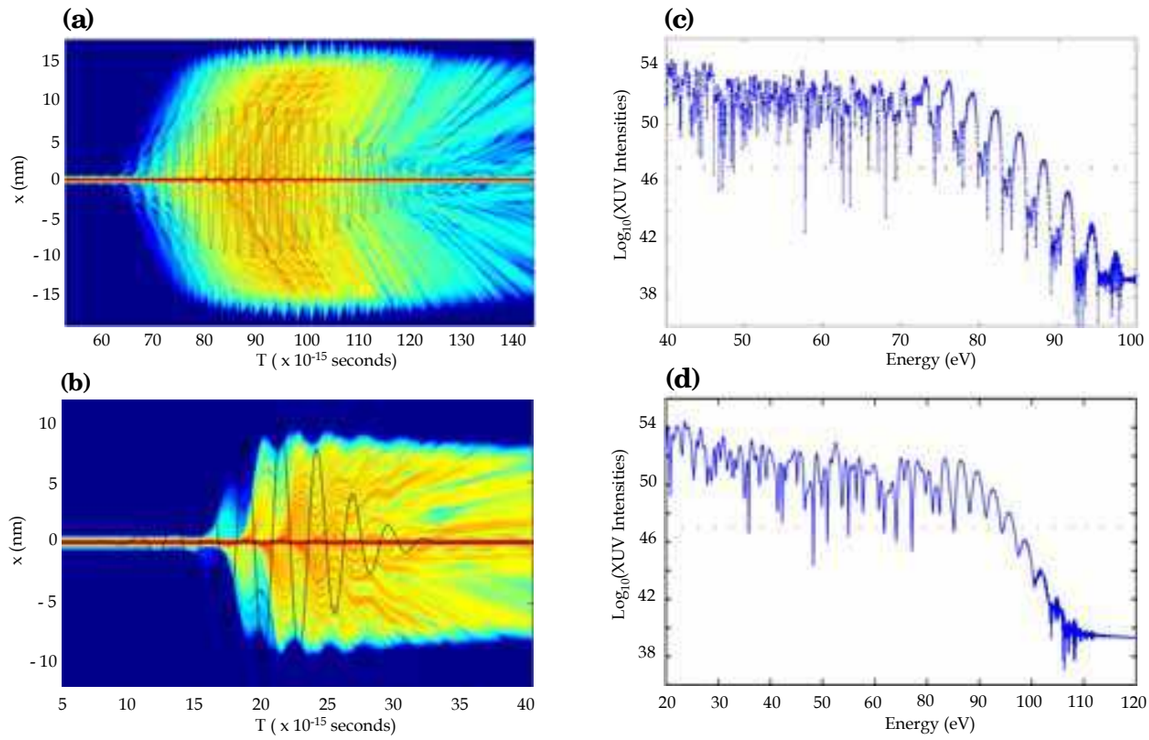

Fig. 2. Solutions to the 1D time-dependent Schrödinger equation. (a) and (b) are $\log_{10}$ (electron density) plotted as a function of x and time, t for 30 fs and 7 fs laser pulses which are also shown. Performing a Fourier transformation on (a) and (b) yields the corresponding high harmonic spectra shown in (c) and (d).

significant portion remains bound to the parent ion. Once in the continuum the ionised portion of the wavefunction undergoes acceleration. Upon returning to the core, it subsequently interferes with the bound part which sets up an oscillating dipole. The result of this oscillation is the emission of the SXR photons. As with the semi classical model a multi cycle laser pulse will result in a series of bursts of SXR photons which will typically result in the characteristic high harmonic spectrum and a train of sub-femtosecond XUV pulses. Comparing figures 2(c) and (d), the individual harmonics are much better defined in the case of a 35 fs, as compared to a 7 fs, duration laser pulse which is consistent with this argument. Reducing the pulse duration still further to the few-cycle regime (corresponding to a pulse duration to 3 fs) a single XUV burst would be expected with the resulting spectrum shown in figures 3 (a) and (b) respectively. In contrast to the calculated harmonic spectra in figures 2 (c) and (d), there is no clear harmonic structure shown to arise from a few-cycle 3 fs pulse, figure 3 (b). Unlike multi-cycle laser pulses, few-cycle laser pulses are used in conjunction with spectral filtering to produce isolated SXR pulses. Currently the record for the shortest duration single SXR pulse produced via laser-driven high harmonic generation stands at 80 as (Goulielmakis et al., 2008). These isolated, sub-femtosecond duration pulses are essential for the investigations into electron dynamics (Kling et al., 2008), time-resolved inner shell spectroscopy (Drescher et al., 2002) and electron correlations (Hu & Collins, 2006) in real time.

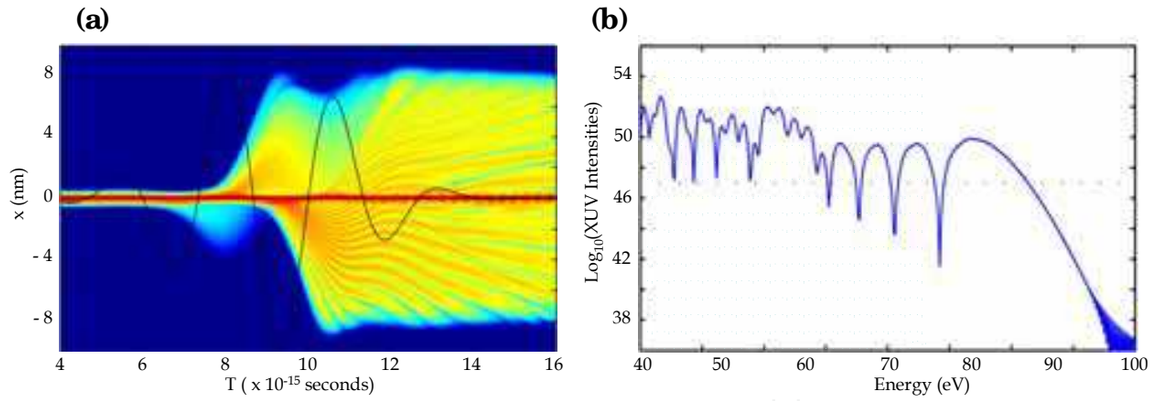

Fig. 3. (a) Few-cycle laser pulse leading to a single SXR photon burst and (b) the resulting spectrum. The shading indicates the part of the spectrum that is filtered in order to produce an isolated attosecond SXR pulse.

For the purposes of imaging sub-micron objects a train of sub-femtosecond XUV pulses is sufficient provided the train is no longer than 10 fs. As long as this is the case then the object that is being imaged will not have sufficient time to undergo Coulomb explosion and fragmentation while in the intense XUV field (Neutze et al., 2000). The configuration and operating parameters of the attosecond SXR nanoprobe is discussed in the following section.

3. Experimental realisation

3.1 Laser source

The experimental system comprises of two parts: the source and generation. As these are independent of one another any improvements in the technology of one can be easily incorporated into the full system.

A commercial Ti: Sapphire chirped pulse amplication (Spitfire Pro, Spectra Physics) laser system is used to produce 3 mJ pulses of duration between 35 – 45 fs at a central wavelength of 790 and 1 kHz repetition rate, a schematic of which is shown in figure 4. The diagnostics used to characterise this output consists of a FROG (***f***requency ***r***esolved ***o***ptical ***g***ating) and a home-built M^2 meter (Praeger 2008). Following characterisation, the beam can either be used to drive the two high harmonic generation lines (denoted 1 and 2) or undergo further compression via filamentation as shown in figure 4.

Filamentation is a straightforward technique that is used to compress intense femtosecond laser pulses. The laser is focused into a 1 m long cell filled with approximately 1 bar of argon gas. As it propagates through the gas it undergoes competing effects in the spectral regime: self focusing from the $\chi^{(3)}$ Kerr effect and self-defocusing due to the plasma index,

$$n_{plasma} = \sqrt{1 - \frac{\omega_p^2}{\omega^2}} \tag{4}$$

where n_{plasma} = plasma refractive index, ω and ω_p are the radiation and plasma frequecies respectively. Likewise, in the time domain the laser pulses undergo broadening and blue shifting due to the ionisation of the surrounding gas which competes with the simultaneous recompression from the gas dispersion effects. Provided the balance between these

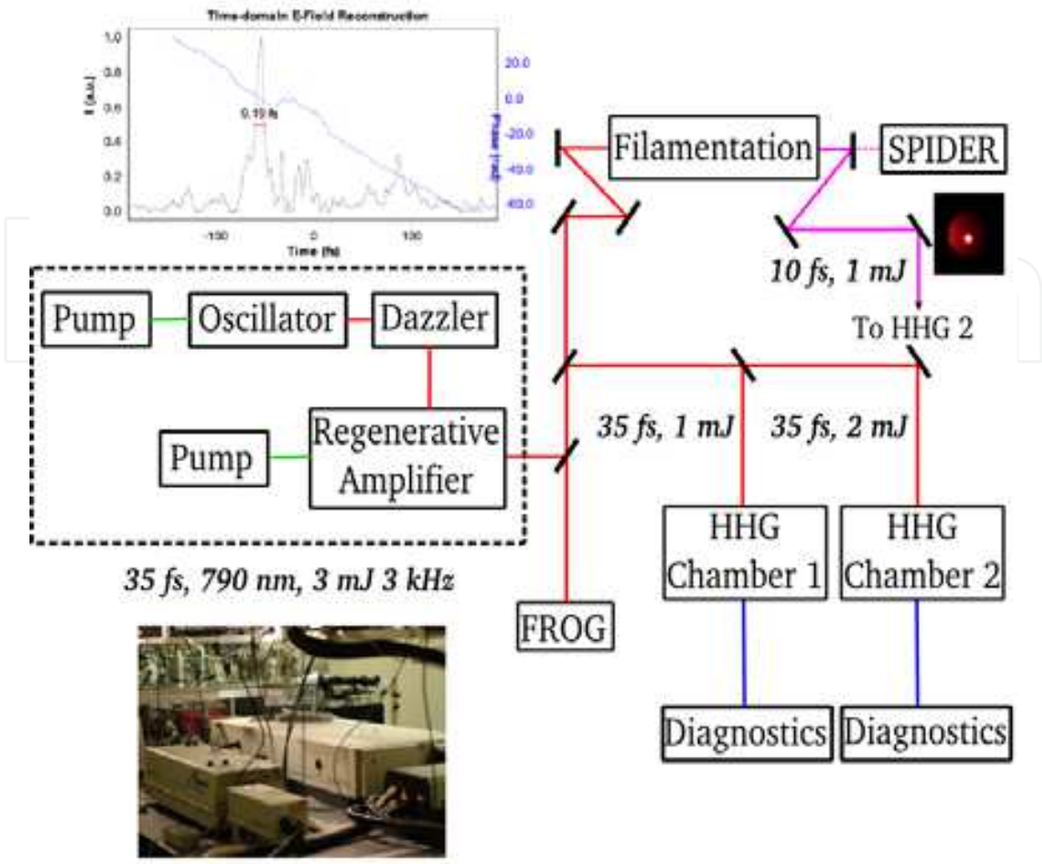

Fig. 4. Laser source used to generate a 10 fs train of sub-femtosecond duration pulses in the XUV for scattering and diffraction imaging. Also shown is the laser mode after filamentation and the corresponding pulse duration measurement in the time domain.

competing processes in both the spectral and temporal domains is correct it is possible to produce spectrally broad pulses of only a few femtosecond duration (Hauri et al., 2005). The filamentation set-up shown in figure 4 is able to produce 10 fs pulses over a spectral range of 450 – 900 nm which are characterised using SPIDER (***s***pectral ***p***hase ***i***nterferometry for ***d***irect ***e***lectric-field ***r***econstruction). Work is on-going to stabilise this output and use it in a number of high harmonic generation experiments. Ultimately the aim is to use these compressed pulses in conjunction with quasi phase matching techniques to access the water window (Gibson et al., 2003). However, for the work presented in the remainder of this chapter, the uncompressed output from the regenerative amplifier i.e. 35 – 45 fs duration pulses were used to drive the high harmonic generation process.

3.2 Capillary high harmonic generation

While laser-driven high harmonic generation has been investigated in a number of different experimental configurations including gas cells (Sutherland et al., 2004; Kazamias et al., 2003; Tamaki et al., 1999), gas jets (Levesque et al., 2007; Paul et al., 2001) and combined capillary and jet geometries (Heinrich et al., 2006), it is SXR production from a single capillary waveguide that is discussed here.

35 fs, 1 mJ laser pulses are focused into a hollow capillary waveguide of 7 cm length and inner diameter of 150 μm to give a peak intensity in excess of 10^{14} W/cm^2. A pair of two 300 μm diameter holes were drilled 2 cm from either end of the waveguide that allow gas, typically argon, to be fed into the capillary and defining a central region of constant pressure.

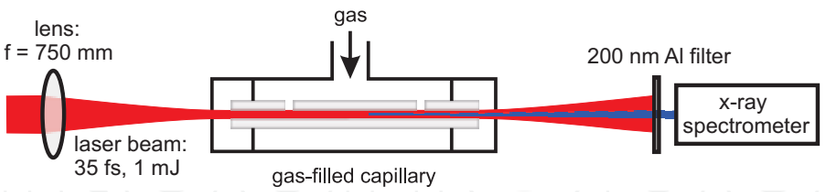

Fig. 5. Schematic of laser-driven high harmonic generation within a capillary waveguide. Reproduced with permission from the Institute of Physics Publishing Ltd (Stebbings et al., 2008).

As both the laser and SXR beams are collinear, a 200 nm aluminium filter is used to block the laser while allowing approximately 10% of the SXRs to be transmitted. This can subsequently be characterised using a grazing incidence spectrometer, Andor x-ray CCD camera or focused and used for scattering and diffraction experiments.

In this configuration the generation process produces SXRs in a coherent and well collimated beam which has a 1 mrad divergence. This output is loosely tunable over a wavelength range of 18 – 40 nm and has approximately 10^7 to 10^8 SXR photons per pulse per harmonic at a repetition rate of 1 kHz under optimal conditions. This equates to an 1μW and 100 kW average and peak powers respectively.

In order to obtain these optimal conditions, and therefore maximise the SXR flux, the phase mismatch, Δk, between the collinear laser and SXR beams must be minimised according to equation 5.

$$\Delta k = q k_{\lambda} - k_{q} \tag{5}$$

Where q = harmonic order, k_{λ} and k_q are the wavevectors of the laser and SXR beams respectively. Phase matching in a capillary is achieved via the relative balance between the refractive indices of the waveguide, neutral gas and plasma. Consequently the amount of ionisation within the capillary plays a critical role due to its influence on the amount of plasma generated as well as the propagating laser beam (Froud et al., 2006). Too little ionisation and no tunnelling, while too much result in a large phase mismatch, Δk - both cases will result in a significant depletion in the observed SXR flux.

In order to improve understanding of SXR production and therefore optimise the source for maximum flux via phase matching, it is essential to characterise the beam and predict the effects such as gas pressure, species and laser propagation have on the flux produced. These aspects were investigated in some detail and are described in following sections.

4. SXR characterisation: spatio-spectral beam imaging

Although physical processes such as phase matching and beam propagation play a fundamental role in laser-driven high harmonic generation, they are complex effects that must be understood before the full potential of capillary waveguides as SXR sources can be realised. With this in mind a novel technique that permits the full characterisation of the SXR in the spectral and spatial domains from a single SXR diffraction image has been developed.

The experimental configuration was based on figure 5 but with two significant differences:

1. A grid supported 200 nm thick aluminium filter. The grid consisted of 38 μm nickel wires that defined a series of 335 μm square aluminium apertures that provided the diffracting object.

And

2. An Andor CCD camera (instead of a grazing incidence spectrometer) that was used to record the image of the entire SXR beam.

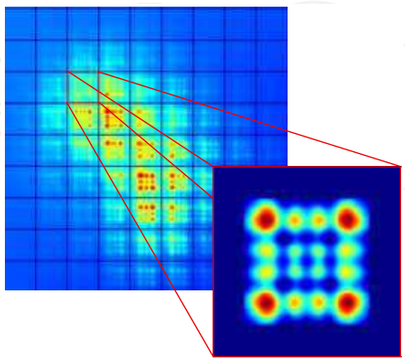

Fig. 6. Fresnel diffraction image of the entire SXR beam generated from 60 mbar of argon gas within a capillary waveguide. The inset shows the diffraction from one aluminium square aperture. This varies as a function of aperture position and is a convolution of a number of different SXR wavelengths. See also (Praeger et al., 2007).

The distances between the SXR source (exit of the capillary waveguide) and the filter and the filter and the camera (defined as the image plane) were 50 cm and 100 cm respectively - well within the Fresnel diffraction regime.

As before the laser (30 fs, 1 mJ, 780 nm) was focused into the capillary waveguide to give peak intensities in excess of 10^{14} W/cm^2. Argon gas was then fed into the system to give a constant pressure equal to 60 mbar within the central region of the capillary. The filter again blocked the laser while allowing approximately 10% of the SXRs to be transmitted and subsequently imaged by the camera over 100 laser shots as shown in figure 6. The image shown in figure 6 was recorded over 100 laser shots corresponding to a total time of 100 ms. Although there is an overall intensity distribution in the SXR beam it is the diffraction from the individual apertures created by the nickel mesh that is of most interest. By examining the image in figure 6 it becomes clear that there is a strong spatial dependence in the diffraction from the aluminium square apertures. Furthermore the source is known to produce a series of harmonic orders (Froud et al., 2006). This means each of these patterns is a convolution of number of different SXR wavelengths. In order to extract any useful information from this image the contributions of each wavelength must be deconvolved from the diffraction pattern from each aperture. Fortunately a number of reasonable assumptions can be made to make these calculations easier.

1. Treat the diffraction from each aperture separately as any contributions from neighbouring apertures are negligible. This is reasonable as photons arriving at any particular point on the image plane are more likely to have taken a direct rather than an indirect path by more than three orders of magnitude.
2. Neglect the spectral width of the harmonics, as any interference between the harmonic will be averaged out over the exposure time of the camera.

The diffraction pattern from each aperture is then calculated using Fresnel theory (Born & Wolf, 1999) for each SXR wavelength up to the 51 st harmonic order that corresponds to a

wavelength of approximately 15 nm. This upper limit is defined by the calculated cut-off energy, E_{max}, given in equation (1). The contributions to the overall diffraction pattern from each aperture are then added as an incoherent sum according to equation 6. (Praeger et al., 2007)

$$P_m(x,y,i,j) = \sum_{h=1}^{\infty} P_c(x,y,i,j,h) I(i,j,h) \tag{6}$$

Where (x, y) are the spatial co-ordinates of the aperture (i, j), h is an odd integer representing the high harmonic orders, P_c and P_m are the calculated and measured diffraction patterns respectively. $I(i, j, h)$ is the weighting factor which is directly proportional to the spectral intensities of each harmonic order. Knowing the measured spectrum, P_m, from one aperture allows linear algebra to be applied in order to determine the weighting factors to give the best fit to the experimental data. Ultimately this allows the reconstruction of the high harmonic spectra that are compared to previously measured data using the grazing incidence spectrometer under similar experimental conditions as shown in figure 7.

In contrast to the camera, the spectrometer is only able to image a small section of the overall SXR beam at any one time. It is possible to scan the spectrometer over the entire beam but maintaining accurate alignment is extremely challenging. Another issue is the integration times required to obtain the data sets – using the spectrometer this typically takes tens of seconds as compared to the 100 ms needed to record the image in figure 6. Due to the highly nonlinear high harmonic process an extended integration time can encompass significant changes in the SXR output from the capillary waveguide. The slight offset between harmonic peaks and the harmonics of fundamental laser is due to blue shifting of the propagating laser (Froud et al., 2006) though it is not accounted for here.

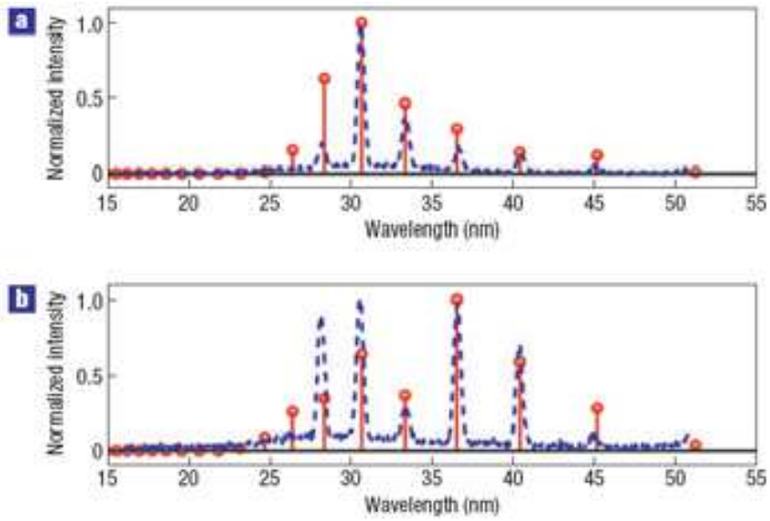

Fig. 7. High harmonic spectra recorded for argon gas pressures of (a) 60 and (b) 80 mbar. Blue dashed and red solid lines denote experimental and reconstructed data respectively. The integration time for the experimental data was 20 seconds. Compare this to the 100 ms required to record the diffraction image in figure 6. Reprinted by permission from Macmillan Publishers Ltd: Nature Physics (Nature Physics 3, 176–179 (1 March 2007), doi:10.1038/nphys516) copyright (2007). (Praeger et al., 2007)
http://www.nature.com/nphys/index.html

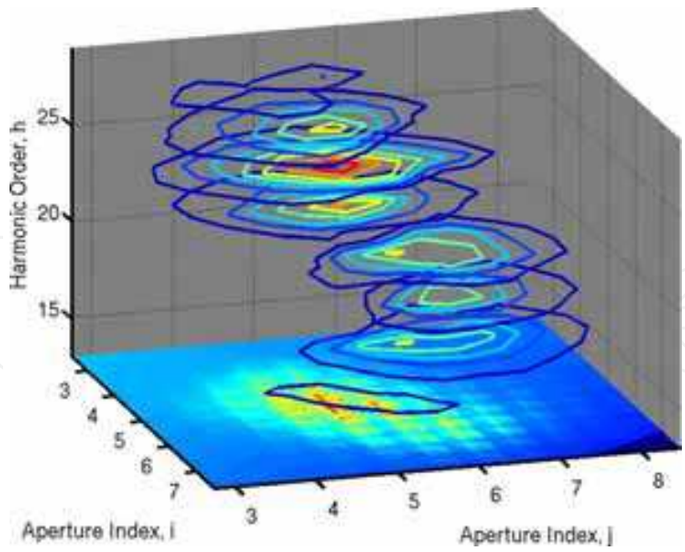

Fig. 8. Spatially resolved reconstructed spectrum for 60 mbar of argon within the capillary waveguide. Coloured lines denote the relative spectral intensities of the harmonic orders. Reprinted by permission from Macmillan Publishers Ltd: Nature Physics (Nature Physics 3, 176–179 (1 March 2007), doi:10.1038/nphys516) copyright (2007). (Praeger et al., 2007) http://www.nature.com/nphys/index.html

Nevertheless there is still good agreement between the reconstructed and the experimental data recorded by the spectrometer in figure 7. While this is a useful comparison and a confirmation of the robustness of the spatio-spectral imaging technique, there is plenty more information that can be extracted from the diffraction image such as the one shown in figure 6. Figure 8 shows the spectral intensity of all of the different SXR wavelengths (as harmonic order of the fundamental laser) as a function of two spatial dimensions corresponding to the aperture indices (i, j). Essentially this is a plot of the spectral intensity of each wavelength spatially across the entire SXR beam generated from the capillary waveguide.

Further information can be extracted from the diffraction image in order to compare the transverse spatial intensity profiles as a function of harmonic order and gas pressure recorded at 60 and 160 mbar respectively. The spatial profiles are all broadly cylindrical symmetric with the high order harmonics (shortest SXR wavelengths) as a spot located close to the centre of the capillary waveguide. The lower orders are located further out and typically show an annular shaped profile. Possible reasons for these observations, including noncollinear and changes in the radial phase matching conditions are discussed in an earlier publication and the reader is referred therein (Praeger et al., 2007).

One of the major benefits of the technique presented here is that a significant amount of spatial and spectral information of the SXR beam can be obtained from one diffraction image. Although the image in figure 6 was recorded over 100 ms, it would be possible to obtain the same information from a single laser shot provided the signal to noise ratio was good enough. Operation in single shot mode opens up applications such as the study of transient phenomena in the high harmonic generation process and the elimination of shot-to-shot noise arising from the laser system.

For the purposes of this chapter however, these results have provided valuable insight into the radial distribution of capillary high harmonic generation and prompted further investigations into the radially dependent SXR production.

5. Molecular variation of capillary-produced SXRs

There are a number of factors that have a significant effect on the SXR production from the laser-driven high harmonic generation process. Not least the propagation geometry of the driving laser field is of critical importance in obtaining ideal phase matching conditions. In gas jets this is achieved via the Guoy phase shift and is limited by the confocal parameter of the focused laser. In contrast capillaries provide an extended interaction length between the laser and the gas media implying the amount of ionisation within the waveguide will profoundly affect the SXR output. This is due to its effects on the propagation of the laser mode and the phase matching via the changes in the refractive index of the plasma generated.

Building on the previous experiments such as those described in section 4, the SXR production was investigated from a number of media of increasing complexity – argon, nitrogen and nitrous oxide – as a function of gas pressure using the experimental configuration shown in figure 5.

In addition a simple spatially and temporally dependent phase matching model was developed in order to predict the overall spectral envelopes of the harmonic spectra without the need for invoking complex quantum mechanical calculations. This is an extension to the phase matching theory originally proposed by Durfee and co-workers (Durfee et al., 1999). As shown in the previous section SXR production in a capillary displays a strong spatial dependence. Although previous work (Durfee et al., 1999) allowed for the radial dependence of ionisation across the capillary in the laser propagation via modal averaging, the variation in radial phase matching conditions was not included. However as the Rayleigh range of the SXRs is long compared to the interaction then SXRs produced at different radii within the capillary will not necessarily interfere. This means that there will be different phase matching criteria as a function of time ***and*** position across the waveguide that are allowed for in the extended phase matching model described here.

The driving laser pulse is assumed to have a Gaussian temporal profile and propagate through the capillary waveguide in the EH_{11} mode (Marcatili & Schmeltzer, 1964), which allows the calculation of the spatially and dependent ionisation using the so-called ADK tunneling theory (Ammosov et al., 1986; Popov, 2004). This is then used to calculate the phase mismatch, Δk, according to equation 7. (Stebbings et al., 2008)

$$\Delta k \approx \frac{q u_{ij} \lambda_0}{4\pi a^2} + N_e r_e \left(q\lambda_0 - \lambda_q\right) - \frac{2\pi N_{atm}}{\lambda_q}\left(\delta(\lambda_0) - \delta\left(\lambda_q\right)\right) \tag{7}$$

Where q is the harmonic order, u_{ij} is the i^{th} root of the Bessel function, J_{i-1}, with i and j both equal to 1 denoting the EH_{11} mode, λ_0 and λ_q the wavelengths of the laser and harmonic (order q) respectively, a is the capillary radius, N_e is the number of electrons, r_e the classical electron radius, a is the radius of the capillary waveguide, N_{atm} the number of neutral gas atoms (or molecules), P is the gas pressure, $\delta(\lambda_0)$ and $\delta(\lambda_q)$ are the dispersion of the neutral gas at the laser and harmonic wavelengths respectively.

The phase mismatch is then substituted into equation 8 in order to determine the intensity as a function of position, r, time, t, and harmonic order, q. (Stebbings et al., 2008)

$$I(r,t,q) \propto dN\left(\frac{1 + e^{-\alpha L} - 2e^{-\alpha L}\cos(\Delta k L)}{\alpha^2 + \Delta k^2}\right) \tag{8}$$

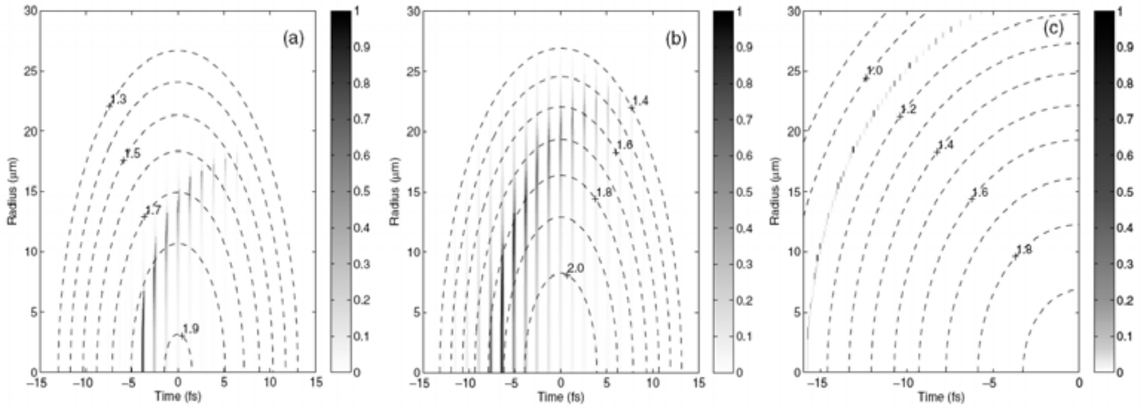

Fig. 9. Theoretical intensity distribution, $I(r, t, q)$, summed over all harmonic intensities for (a) argon, (b) nitrogen and (c) nitrous oxide. The dashed lines denote the iso-intensity contours which are multiplied by 10^{14} W/cm^2. The maximum intensity has also been normalised to 1. Reproduced with permission from Institute of Physics Publishing Ltd (Stebbings et al., 2008).

Where dN is the number of ions produced in a given time interval, α is the field attenuation coefficient and L is the length of the capillary waveguide. $I(r,t,q)$ can then be plotted as a function of time and capillary radius as shown in figure 9.

Figure 9 (a) shows the theoretical phase matched SXR build up from argon gas. Significant intensity is predicted over intensities from 1.6 to 1.8 x 10^{14} W/cm^2 and out to a capillary radius, r = 20 μm. Initially the intensity starts to build up on the rising edge of the laser pulse at t = -5 fs, close to the centre of the waveguide. As the laser intensity increases with time, the phase matched SXR production is pushed out to larger radii. This effect is due to the increasing ionisation fraction along the central core of the waveguide. There is no SXRs observed beyond r = 20 μm and -5 fs ≤ t ≤ 10 fs as the laser intensity is too low.

Similar trends are also observed for nitrogen shown in figure 9 (b). In contrast to argon however, phase matched SXRs are seen to laser intensity, I = 1.4 x 10^{14} W/cm^2 due to higher ionisation fractions being produced earlier in the pulse, and out to a radius, r = 25 μm. These observations are consistent with the lower ionisation potential of nitrogen as compared to argon.

The results from nitrous oxide, figure 9 (c), are significantly different from either argon or nitrogen. The SXRs are highly localized over laser intensities from 1 to 1.2 x 10^{14} W/cm^2 implying only a small fraction of the driving laser pulse is exploited. These observations are in part explained by the differences in the ionisation properties of nitrous oxide as compared to argon and nitrogen, though other properties such as the quantity of neutral gas and plasma will also play a significant role.

The SXR spectra for argon, nitrogen and nitrous oxide were measured over a pressure range of 5 to 200 mbar. By calculating $I(r, t)$ for each harmonic order, q, a direct comparison between the measured data and theory can be achieved. A selection of these results is shown in figure 10. For further data sets please refer to (Stebbings et al., 2008). Also shown for completeness are the predicted curves using the original phase matching theory (Durfee et al., 1999).

The spatial and temporal theory predicts the overall shape of the spectral envelope and cut-off well for argon and nitrogen for a variety of pressures up to 70 mbar showing a marked

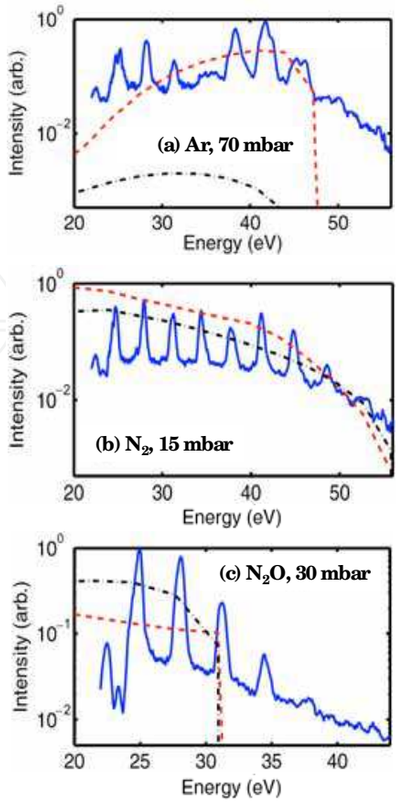

Fig. 10. Selection of experimental SXR spectra for (a) argon, (b) nitrogen and (c) nitrous oxide for different gas pressures as shown by the solid blue lines. The dashed red and blue dashed-dotted curves denote the extended and original phase matching theories. Reproduced with permission from Institute of Physics Publishing Ltd. (Stebbings et al., 2008)

improvement over the previous theory. This agreement decreases for higher pressures as there are a number of complex effects including broadening and splitting of the harmonics. It is also proposed that high pressures can cause temporal distortions in the laser pulse. As these effects lie outside the scope of the simple phase matching theory here it is not surprising that the agreement with the experimental data decreases with increasing pressure.

The predicted cut-off according to equation 1 for argon and nitrogen is 50 eV which is significantly lower than that observed experimentally for most experimental pressures investigated. The reasons for these differences are attributed to absorption of the SXRs by the gas medium as well as phase matching effects, neither of which is accounted for in equation 1. Only by including phase matching can a match between the theoretical and experimental cut-off be achieved highlighting the importance of phase matching effects in capillary high harmonic generation.

In contrast both theories are unable to predict the spectral envelopes arising from high harmonic generation in nitrous oxide an example of which is shown in figure 10 (c). The phase matching calculations are extremely sensitive to the amount of ionisation. Unfortunately this fraction was determined using ADK theory which is an atomic tunneling theory and therefore not ideally suited to a triatomic molecule.

The improvement in agreement between the extended phase matching theory and the experimental data highlights the importance of including spatially and temporally

dependent ionisation within the capillary waveguide. However further developments including the incorporation of pressure dependence in the laser pulse profile and a rigorous tunneling theory for triatomic molecules would yield further improvements. Furthermore it should help researchers achieve optimal conditions for SXR production from a capillary waveguide.

6. Determination of the complex refractive index of sub-micron nanospheres in the SXR region

Table-top sources of SXR radiation offer the potential for unprecedented insight into attosecond dynamics with sub-micron spatial resolution. The high flux (ranging from 10^8 – 10^{11} photons per harmonic per second depending upon generation conditions) and excellent coherence of the SXR beam has opened up many new areas for the analysis of nanoscale objects and systems. In this section the source was used to provide a direct measurement of the complex refractive index of polystyrene spheres within the SXR region.

The nanospheres (average diameter of 194 nm with an uncertainty of < 5 %) were deposited on a 50 nm thick silicon nitride membrane (Duke Scientifics, 1.05 g/cm^3) to form a well ordered, single layer hexagonal close packed array as shown in figure 11. Although the ordering was good it was not perfect and a number of defects can be seen in the array in figure 11.

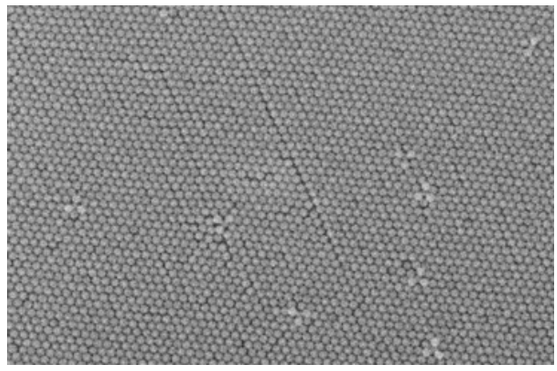

Fig. 11. Scanning electron microscope image of self assembled nanospheres.

In contrast to earlier experiments, laser pulses of 40 fs duration, 1.5 mJ energy at a central wavelength of 800 nm and 1 kHz repetition rate were focused with a dielectric mirror (f = 500 mm) into a gas cell containing 10 mbar of argon. As before the laser and SXR beams were collinear with the laser being blocked by two 100 nm thick aluminium filters. These allowed the transmission of the SXRs to the interaction chamber as shown in figure 12. The SXR beam was subsequently focused by a MoSi multilayer mirror to a spot of 22 μm diameter. The 2D array of nanospheres was placed at the focus and the scattered SXRs detected in transmission by an x-ray CCD camera (Andor, 1024 x 1024 pixels where 1 pixel = 13.5 μm) in the far field regime.

The recorded diffraction pattern in figure 13 shows a number of interesting features. The first of these is in the radial direction where there are multiple spots. These spots were thought to arise from the diffraction of the multiple harmonic wavelengths making up the SXR beam. This was confirmed by removing the MoSi mirror and measuring the spectrum of the SXR beam, which was found to have a wavelength range of 35 – 24 nm

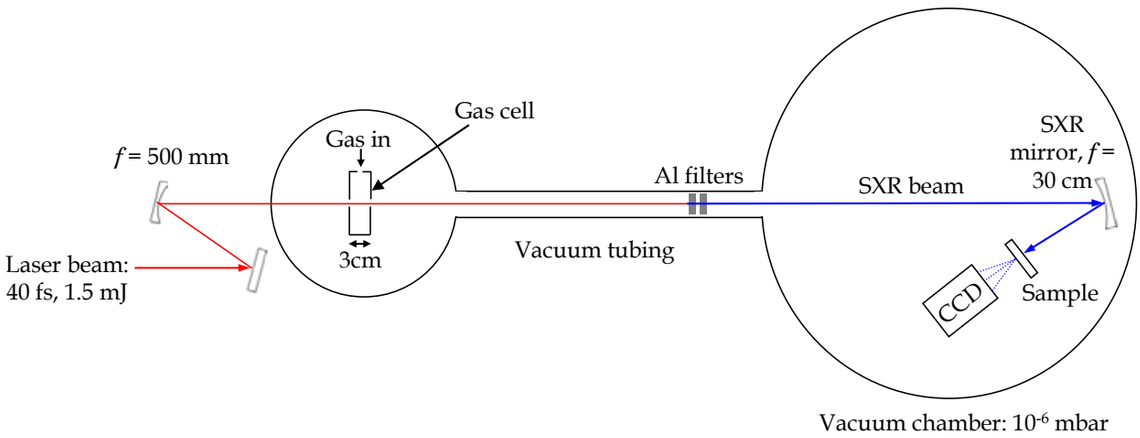

Fig. 12. Schematic of the experimental configuration employed to determine the complex refractive index of a 2D array of 194 nm diameter polystyrene spheres. This set-up is described in detail in (Mills et al., 2008).

(corresponding to photon energies of 36 – 51 eV respectively). The separation of these wavelengths matched the separation of the radial diffraction spots observed in figure 13. Other features include the lack of rotational symmetry and the broadening in the axial direction of the diffraction image. In the experimental configuration (figure 12), the spherical SXR mirror was used in an off-axis geometry. This resulted in a curved wavefront at the focus which led to the lack of rotational symmetry observed in the diffraction image. The broadening in the axial direction was attributed primarily to the defects in the 2D nanosphere array (some of these can be seen in figure 11).

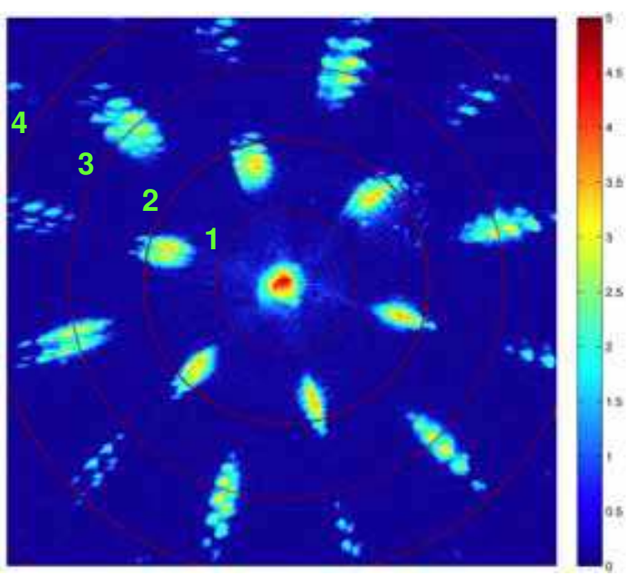

Fig. 13. Far field diffraction pattern from the 2D hexagonal close packed array of 194 nm polystyrene spheres. The integration time was 240 seconds and the intensity is on a logarithmic scale. The red circles denote the angle of 100 mrad x *n* where *n* is the contour number. Reprinted and adapted (original in black and white) from (Mills et al., 2008).

The diffraction image shown in figure 13 is the scattering function from a single sphere multiplied by an array of delta functions. Therefore the image can be thought of as sampling the angular distribution of SXR light scattered from a single sphere. This can be determined analytically using Mie theory and is dependent upon the size (for a spherical object this is the radius) of the scatterer, its complex refractive index and the wavelengths of the incident SXR light. As the wavelengths and radius are known, it is possible to use Mie theory to determine the complex refractive index (equation 9), n_c, of the polystyrene spheres within the SXR region of the electromagnetic spectrum.

$$n_c = \alpha + i\beta \tag{9}$$

Where α and β are parameters to be determined. These parameters were found from the diffraction image, recorded in figure 13, by measuring the intensity of the SXR wavelength as a function of angle. A linear least square fitting routine was then used to fit the Mie and measured diffraction peak intensities for the first three scattering orders. The results are shown for a SXR wavelength of 27.6 nm in figure 14.

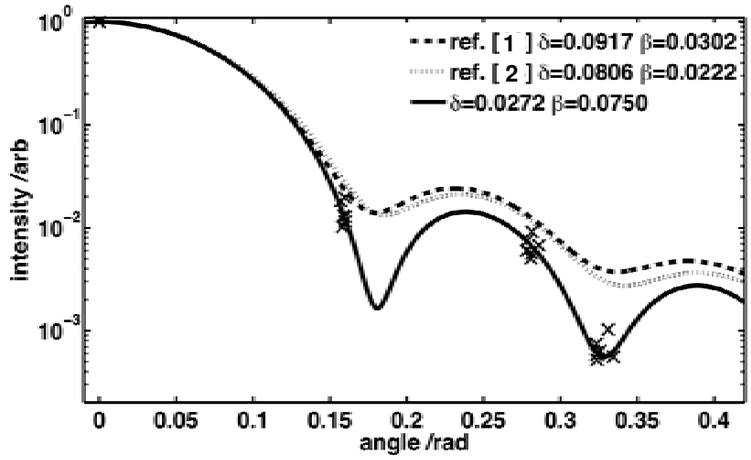

Fig. 14. Comparison between the Mie scattering theory (solid line) for light scattered from a single sphere and the experimental diffraction peaks for a SXR wavelength of 27.6 nm and with complex refractive indices from (dashed line, ref [1] in figure) NIST, Chantler et al., and (dotted line, ref [2] in figure) the Centre for X-ray Optics and determined from the work presented here (solid black line). Reprinted with permission from (Mills et al., 2008).

The complex refractive index parameters, α and β, of this and other SXR wavelengths (26.9 and 29.6 nm) were determined and compared to extrapolated data from CXRO (Centre for X-ray Optics) and NIST (National Institute of Standards and Technology, Chantler, et al.) as shown in figure 15.

Although the general trend of the extrapolated curves follows the experiment, there is a large discrepancy between the magnitudes thus highlighting the importance of obtaining experimental data within this region (Mills et al., 2008).

Using a single diffraction image, the technique described here can be extended to other SXR wavelengths and many other nanostructures provided they are periodic and will therefore diffract light in a manner that is dependent upon their complex refractive indices.

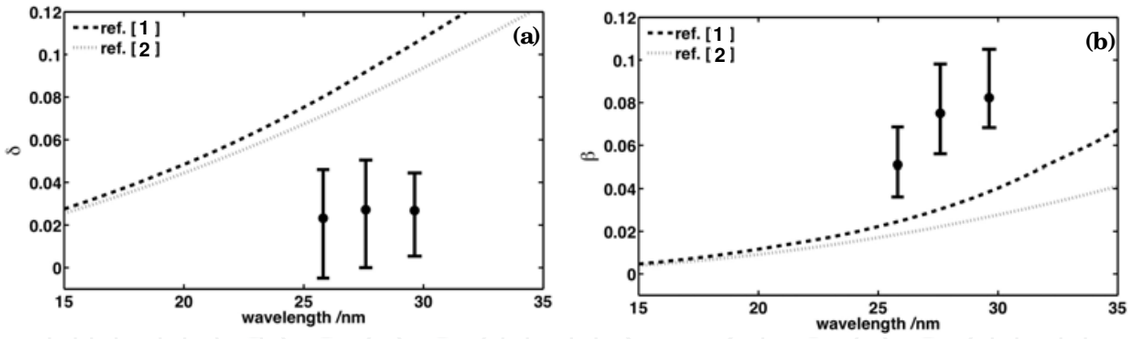

Fig. 15. Comparison of the experimentally determined and extrapolated [1] CXRO and [2] NIST (Chantler, et al., 1995) data for (a) α and (b) β. Reprinted with permission from (Mills et al., 2008).

7. Future work & summary

The table-top, laser-driven SXR source described here routinely produces a total flux of approximately 10^8 photons per harmonic per second at 1 kHz repetition rate to give approximately 1 μW average and 100 kW peak powers respectively. The SXR beam itself has a high spatial coherence and is well-collimated with a divergence of < 1 milli radian. Typically the SXRs have wavelengths from 18 – 50 nm which are loosely tunable depending upon the generation conditions within the capillary waveguide.

The investigation of SXR production from molecular gases e.g. N_2 and N_2O were of particular interest as they provided different combinations of gas absorption, index and ionisability with which to change the spectrum of the emitted SXR radiation. Several interesting effects were observed in the SXR spectra (figure 10 and references therein) that combine the effects of phase matching and the propagation of the driving laser beam. Only by developing a model that incorporates the change in ionisation within the waveguide as a function of time within the laser pulse and radial distance across the capillary could the SXR spectral envelope be predicted.

In order to understand the effects of capillary propagation of the generated SXRs, several diagnostic techniques have been developed and described in this chapter. Using the Ni grids which act as a support for the 200 nm thick free-standing aluminium filter (used to separate the SXR and laser beams) significant spectral and spatial detail of the SXR beam has been observed. Fresnel diffraction from each grid square was used to reconstruct the spectrum within each square leading to a 2D spectral profile across the beam. An understanding of the beam is critical to understand the effect of the radial distribution of ionisation on the SXR production and for further optimisation of the overall SXR flux.

Initial scattering investigations from an array of sub-micron latex spheres have proved extremely successful. The results from these experiments have demonstrated the direct measurement of the complex refractive index of polystyrene nanosphers by analysis of the resulting SXR diffraction intensity distribution. This technique further demonstrates the applicability of a high harmonic SXR source for nanoscale analysis and can be extended to determine the complex refractive index of a material for a range of wavelengths from one diffraction image. These investigations will be extended to other periodic nanostructures in order to gain new insights as well as test the applicability of the technique. The technique of

coherent diffraction imaging, CDI, is currently being tested and applied to the SXR diffraction image (figure 13) in order to reconstruct the 2D hexagonal close packed array of polystyrene spheres (figure 11). Future work will combine the technique of coherent diffraction imaging (Gerchberg & Saxton, 1972; Fienup, 1978) with experimental SXR diffraction in order to reconstruct the overall conformation and shape of a wide variety of nanoscale objects.

In the long-term, the plan is to combine quasi phase matching techniques (Gibson et al., 2003) with compression of the driving laser pulse from 40 to 10 fs duration in order to access the water window. Once this regime is reached, further SXR scattering experiments will be carried out. The analysis of the resulting SXR diffraction patterns (via coherent diffraction imaging) will permit the shape of sub-micron objects such as biological molecules within their native, aqueous environments to be determined.

8. References

Ammosov, M. V.; Delone, N. B. & Krainov, V. P. (1986). Tunnel ionization of complex atoms and of atomic ions in an alternating electromagnetic field. *Soviet Physics - JETP*, 64, 1191 - 1194

Beale, T. A. W.; Bland, S. R.; Johnson, R. D.; Hatton, P. D.; Cezar, J. C.; Dhesi, S. S.; Zimmermann, M. V.; Prabhakaran, D. & Boothroyd, A. T. (2009). Thermally induced rotation of 3d orbital stripes in $Pr(Sr_{0.1}Ca_{0.9})_2Mn_2O_7$. *Physical Review B, Condensed Matter and Materials Physics*, 79, 5, (February 2009) 054433-1 - 054433-5, ISSN 1550-235x (online), 1098-0121 (print)

Bogan, M. J.; W. Benner, H.; Boutet, S.; Rohner, U.; Frank, M.; Barty, A.; Seibert, M. M.; Maia, F.; Marchesini, S.; Bajt, S.; Woods, B.; Riot, V.; Hau-Riege, S. P.; Svenda, M.; Marklund,E.; Spiller,E.; Hajdu, J. & Chapman, H. N. (2008). Single Particle X-ray Diffractive Imaging. *Nano Letters*, 8, 1, (January 2008) 310 - 316, ISSN 1530-6992 (online), 1530-6984 (print)

Born, M. & Wolf, E. (1999). *Principles of Optics, Theory of Propagation, Interference and Diffraction of Light*, Cambridge University Press, 0521642221, Cambridge UK.

Centre for X-ray Optics, http://henke.lbl.gov/optical_constants/getdb2.html.

Chantler, C. T.; Olsen, K.; Dragoset, R. A.; Chang, J.; Kishore, A. R.; Kotochigova, S. A. & Zucker, D. S. X-ray form factor, attenuation and scattering tables (version 2.1). http://physics.nist.gov/ffast, National Institute of Standards and Technology, Gaithersburg, MD.

Corkum, P.B. (1993). Plasma perspective on strong field multiphoton ionization. *Physical Review Letters*, 71, 13, (September 1993) 1994 - 1997, ISSN 1079-7114 (online), 0031-9007 (print)

Drescher, M.; Hentschel, M.; Kienberger, R.; Uiberacker, M.; Yakovlev, V.; Scrinzi, A.; Westerwalbesloh, Th.; Kleineberg, U.; Heinzmann U. & Krausz, F. (2002). Time-resolved atomic inner-shell spectroscopy. *Nature*, 320, 6909, (October 2002) 803 - 807, ISSN 0028-0836

Durfee, C. G.; Rundquist, A. R.; Backus, S.; Herne, C.; Murnane, M. M. & Kapteyn, H. C. (1999). Phase matching of high-order harmonics in hollow waveguides. *Physical Review Letters*, 83, 11, (September 1999) 2187 – 2190, ISSN 1079-7114 (online), 0031-9007 (print)

Froud, C. A.; Rogers, E. T. F.; Hanna, D. C.; Brocklesby, W. S.; Praeger, M.; de Paula, A. M.; Baumberg, J. J & Frey, J. G. (2006). Soft-x-ray wavelength shift induced by ionization effects in a capillary. *Optics Letters*, 31, 3, (February 2006) 374 - 376, ISSN 0146-9592

Fienup, J.; (1978). Reconstruction of an object from the modulus of its Fourier transform. *Optics Letters*, 3, 1, (July 1978) 27 - 29, ISSN 0146-9592

Gerchberg, W. & Saxton, W. O. (1972). A practical algorithm for the determination of the phase from image and diffraction plane pictures. *Optik*, 35, 237 – 246

Gibson, E. A.; Paul, A.; Wagner, N.; Tobey, R.; Gaudiosi, D.; Backus, S.; Christov, I. P.; Aquila, A.; Gullikson, E. M.; Attwood, D. T.; Murnane M. M. & Kapteyn, H. C. (2008). Coherent Soft X-ray Generation in the Water Window with Quasi-Phase Matching. *Science*, 302, 5642, (October 2003) 95 - 98, ISSN 1095-9203 (online), 0036-8075 (print)

Goulielmakis, E.; Schultze, M.; Hofstetter, M.; Yakovlev, V. S.; Gagnon, J.; Uiberacker, M.; Aquila, A. L.; Gullikson, E. M.; Attwood, D.T.; Kienberger, R.; Krausz F. & Kleineberg, U. (2008). Single-Cycle Nonlinear Optics. *Science*, 320, 1614, (June 2008) 1614 - 1617, ISSN 1095-9203 (online), 0036-8075 (print)

Hauri, C. P.; Guandalini, A.; Eckle, P.; Kornelis, W.; Biegert, J. & Keller, U. (2005). Generation of intense few-cycle laser pulses through filamentation – parameter dependence. *Optics Express*, 13, 19, (September 2005) 7541 - 7547, ISSN 1094-4087

Heinrich, A.; Kornelis, W.; Anscombe, M. P.; Hauri, C. P.; Schlup, P.; Biegert, J. & Keller, U. (2006). Enhanced VUV-assisted high harmonic generation. *J Phys. B: At. Mol. Opt. Phys.*, 39, 13, (June 2006) S275 – S281, ISSN 0953-4075 (print) 1361-6455 (web)

Hu, S. X. & Collins, L. A. (2006). Attosecond pump probe: exploring ultrafast electron motion inside an atom. *Physical Review Letters*, 96, (February 2006) 073004-1 – 073004-4, ISSN 1079-7114 (online), 0031-9007 (print)

Humphrey, D. S.; Cabailh, G.; Pang, C. L.; Muryn, C. A.; Cavill, S. A.; Marchetto, H.; Potenza, A.; Sarnjeet S. Dhesi, S. S. & Thornton, G. (2009). Self assembled metallic nanowires on a dielectric support: Pd on rutile TiO_2 (110). *Nano Letters*, 9, 1, (January 2009) 155-159, ISSN 1530-6992 (online), 1530-6984 (print)

Jordan, G. & Scrinzi, A. (2008). Core polarization effects in molecular high harmonic generation. *New Journal of Physics*, 10, (February 2008) 025035-1 – 025035-18, ISSN 1367-2630 (online)

Kazamias, S.; Douillet, D.; Weihe, F.; Rousse, A.; Sebban, S.; Grillon, G.; Augé, F.; Hulin, D.& Balcou, Ph. (2003). Global optimization of high harmonic generation. *Physical Review Letters*, 90, (May 2003) 193901-1 – 193901-4, ISSN 1079-7114 (online), 0031-9007 (print)

Kling, M. F. and Vrakking, M. J. J.; (2008). Attosecond electron dynamics. *Annual Review in Physical Chemistry*, 59, (May 2008) 463-492, ISSN

Levesque, J.; Zeidler, D.; Marangos, J. P.; Corkum, P. B. & Villeneuve, D. M. (2007). High Harmonic Generation and the Role of Atomic Orbital Wave Functions. *Physical Review Letters*, 98, 18, (April 2007) 183903-1 – 183903-4, ISSN 1079-7114 (online), 0031-9007 (print)

Lewenstein, M.; Balcou, Ph.; Ivanov, M. Yu.; C. L.; L'Huillier, A. & Corkum, P. B. (1994). Theory of high harmonic generation by low-frequency laser fields. *Physical Review A*, 49, 3, (March 1994) 2117-12132, ISSN 1094-1622 (online), 1050-2947 (print), 1538-4446 (CD-ROM)

Marcatili, E. A. J. & Schmeltzer, R. A. (1964). Hollow metallic and dielectric waveguides for long distance optical transmission and lasers (long distance optical transmission in hollow dielectric and metal circular waveguides, examining normal mode propagation). *Bell Systems Technology Journal*, 43, (July 1964) 1783-1809, ISSN 00058580

Reprinted with permission from Mills, B.; Chau, C. F.; Rogers, E. T. F.; Grant-Jacob, J.; Stebbings, S. L.; Praeger, M.; de Paula, A. M.; Froud, C. A.; Chapman, R. T.;

Butcher, T. J.; Baumberg, J. J.; Brocklesby, W. S. & Frey, J. G. Direct measurement of the complex refractive index in the extreme ultraviolet spectral region using diffraction from a nanosphere array. 93 (23) 231103-1 – 231103-3 (December 2008). Copyright (2008) American Institute of Physics. ISSN Print + Online: 0003-6951 Online only: 1077-3118

Neutze, R.; Wouts, R.; van der Spoel, D.; Weckert, E. & Hajdu, J. (2000). Potential for biomolecular imaging with femtosecond x-ray pulses. *Nature*, 406, 803, (August 2000) 752-757, ISSN 0028-0836

Paul, P. M.; Toma, E. S.; Berger, P.; Mullot, G.; Augé, F.; Balcou, Ph.; Muller, H. G. & Agostini, P. (2001). Observation of a train of attosecond pulses from high harmonic generation. *Science*, 292, 5522, (June 2001) 1689 - 1692, ISSN 1095-9203 (online), 0036-8075 (print)

Praeger, M.; de Paula, A. M.; Froud, C. A.; Rogers, E. T. F.; Stebbings, S. L.; Brocklesby, W. S.; Baumberg, J. J. & Frey, J. G. (2007). Spatially resolved soft X-ray spectrometry from single-image diffraction. *Nature Physics*, 3, (February 2007) 176-179, ISSN 1745-2473

Praeger, M. (2008). Development and spatio-spectral mapping of a capillary high harmonic source. *Faculty of Engineering*, *Science and Mathematics*, *School of Physics and Astronomy*, University of Southampton, PhD thesis (March 2008)

Popov, V. S. (2004). Tunnel and multiphoton ionization of atoms and ions in a strong laser field (Keldysh theory). *Physics -Usp*, 3, (September 2004) 855-885

Rosenhahn, A.; Staier, F.; Nisius, T.; Schäfer, D.; Barth, R.; Christophis, C.; . Stadler, L-M.; Streit-Nierobisch, S.; Gutt, C.; Mancuso, A.; Schropp, A.; Gulden, J.; Reime, B.; Feldhaus, J.; Weckert, E.; Pfau, B.; Günther, C. M.; Könnecke, R.; Eisebitt, S.; Martins, M.; Faatz, B.; Guerassimova, N.; Honkavaara, K.; Treusch, R.; Saldin, E.; Schreiber, S.; Schneidmiller, E. A.; Yurkov, M. V.; Vartanyants, I.; Grübel, G.; Grunze, M. & Wilhein, T. (2009). Digital In-line Holography with femtosecond VUV radiation provided by the free-electron laser FLASH. *Optics Express*, 17, 10, (May 2009) 8220 - 8228, ISSN 1094-4087

Sandberg, R. L.; Song, C.; Wachulak, P. W. W.; Raymondson, D. A.; Paul, A.; B Amirbekian, B.; Lee, E.; Sakdinawat, A. E.; Voraki, C. La- O-; Marconi, M. C.; Menoni, C. S.; Murnane, M. M.; Rocca, J. J.; Kapteyn, H. C. & Miao, J. (2008). High numerical aperture tabletop soft x-ray diffraction microscopy with 70-nm resolution. *Proceedings of the National Academy of Sciences of the United States of America*, 105, 1, (January 2008) 24 - 27, ISSN 1091-6490 (online)

Schafer, K. J.; Yang, B.; DiMauro, L. F. & Kulander, K. C. (1993). Above threshold ionization beyond the high harmonic cutoff. *Physical Review Letters*, 70, 11, (March 1993) 1599 - 1602, ISSN 1079-7114 (online), 0031-9007 (print)

Stebbings, S.L.; Rogers, E. T. F.; de Paula, A. M.; Praeger, M.; Froud, C. A.; Mills, B.; Hanna, D. C.; Baumberg, J. J.; Brocklesby, W. S. & Frey, J. G. (2008). Molecular variation of capillary-produced soft x-ray high harmonics. *J Phys. B: At. Mol. Opt. Phys.*, 41, 14, (July 2008) 145602-1 - 145602-8, ISSN 0953-4075 (print) 1361-6455 (web) Editor Adrian Corrigan.

Sutherland, J.; Christensen, E.; Powers, N.; Rhynard, S.; Painter, J. & Peatross, J. (2004). High harmonic generation in a semi-infinite gas cell. *Optics Express*, 12, 19, (September 2004) 4430 - 4436, ISSN 1094-4087

Tamaki, Y.; Itatani, J.; Nagata, Y.; Obara, M. & Midorikawa, K. (1999). Highly efficient, phase-matched high-harmonic generation by a self-guided laser beam, 82, 7, (February 1999) 1422 - 1425, ISSN 1079-7114 (online), 0031-9007 (print)

Advances in Solid State Lasers Development and Applications

Edited by Mikhail Grishin

ISBN 978-953-7619-80-0
Hard cover, 630 pages
Publisher InTech
Published online 01, February, 2010
Published in print edition February, 2010

Invention of the solid-state laser has initiated the beginning of the laser era. Performance of solid-state lasers improved amazingly during five decades. Nowadays, solid-state lasers remain one of the most rapidly developing branches of laser science and become an increasingly important tool for modern technology. This book represents a selection of chapters exhibiting various investigation directions in the field of solid-state lasers and the cutting edge of related applications. The materials are contributed by leading researchers and each chapter represents a comprehensive study reflecting advances in modern laser physics. Considered topics are intended to meet the needs of both specialists in laser system design and those who use laser techniques in fundamental science and applied research. This book is the result of efforts of experts from different countries. I would like to acknowledge the authors for their contribution to the book. I also wish to acknowledge Vedran Kordic for indispensable technical assistance in the book preparation and publishing.

INTECH
open science | open minds

InTech Europe
University Campus STeP Ri
Slavka Krautzeka 83/A
51000 Rijeka, Croatia
Phone: +385 (51) 770 447
Fax: +385 (51) 686 166
www.intechopen.com

InTech China
Unit 405, Office Block, Hotel Equatorial Shanghai
No.65, Yan An Road (West), Shanghai, 200040, China
中国上海市延安西路65号上海国际贵都大饭店办公楼405单元
Phone: +86-21-62489820
Fax: +86-21-62489821

IntechOpen